JOURNAL OF CATALYSIS 149, 36–51 (1994)

Dehydration of *n*-Butanol on Zeolite H-ZSM-5 and Amorphous Aluminosilicate: Detailed Mechanistic Study and the Effect of Pore Confinement

M. A. Makarova,*,[1] E. A. Paukshtis,* J. M. Thomas,† C. Williams,*,†,[2] and K. I. Zamaraev*

*Boreskov Institute of Catalysis, Russian Academy of Sciences Siberian Branch, Prospekt Akademika Lavrentieva, 5, Novosibirsk 630090, Russia; and †Davy Faraday Research Laboratory, The Royal Institution, 21 Albemarle Street, London, W1X 4BS, United Kingdom

Received December 1, 1993; revised March 7, 1994

This study of the catalytic dehydration of *n*-butanol on zeolite H-ZSM-5 and amorphous aluminosilicate confirms the reaction scheme proposed earlier by the authors for isobutanol dehydration. The rate constant for *n*-butanol dehydration on H-ZSM-5 (determined from *in situ* FTIR kinetic studies by monitoring the growth of the water deformation peak at 1640 cm^{-1}) is shown to be the true dehydration rate constant (1.7×10^{-4} s^{-1} at 100°C). On the other hand, the rate constants determined from GC steady-state kinetic studies (temperature interval 105–185°C) are effective ones, giving activation energies of 22 ± 2 kcal/mol and 33 ± 2 kcal/mol for complete dehydration and dehydration to butene only, respectively. By studying the dehydration reaction under different conditions (flow and static reactors, steady-state and non-steady-state regimes) and on samples with rather similar acid strengths but different porous systems (H-ZSM-5—microporous channels with diameter ~5.5 Å, and amorphous aluminosilicate—pores of average diameter ~50 Å), it was shown that depending on the concentration of butanol in the immediate vicinity of the active alkoxide intermediate ∃-OC_4H_9, different reaction paths are utilized. High concentrations of alcohol favor ether formation, whereas low ones favour butene. This also explains the so-called "stop effect" observed in GC experiments, where an increase in the rate of butene formation occurs when the flow of alcohol is stopped and replaced with a flow of pure helium. Here, decreasing the concentration of alcohol in the micropores results in more of the alkoxide intermediate transforming to butene rather than to ether (which was the case at steady state).

I. INTRODUCTION

The mechanism of alcohol dehydration on oxide acid catalysts has received considerable attention in the past (1). In the 1960's Knözinger *et al.* developed the consecutive-parallel scheme for alcohol dehydration to olefin and ether—which most successfully described the observed processes (1, 2). Over the last few years interest in these types of reactions, particularly on zeolite catalysts, has again returned. This seems to arise from two factors. On one hand, there has been the development of the methanol to gasoline (MTG) process on ZSM-5 type zeolites (3), and on the other, improved experimental techniques have made the search for reaction intermediates more likely to be successful. Of the latest studies concerned with *n*-butanol dehydration, we note the work of Krampera *et al.* on Al_2O_3 (4), a study of a series of industrial zeolite catalysts by Yue *et al.* (5), the search for reaction intermediates on H-ZSM-5 by Aronson *et al.* (6), and an IR study by Kalvachev *et al.* (7).

The present work on *n*-butanol dehydration is part of a series of studies aimed at understanding the influence of pore confinement in zeolite H-ZSM-5 on the pathways and reaction intermediates of the dehydration reactions of various butanols (8–13), and is a continuation of work reported briefly in Ref. (8). On the basis of the results obtained in the present study, a mechanistic model has been developed for the reaction which allows us to explain all the observed dependences and in particular the "stop effect" (increase in the rate of butene formation after the flow of *n*-butanol to the reactor is stopped and replaced it by pure helium).

In order to study the influence of the micropores on the course of reaction, we have compared the behavior of reactions on (1) zeolites with rather similar concentrations of active sites (bridging OH groups) but different crystallite sizes (to study the influence of diffusion of reactant into the pores) and (2) samples with known, well-defined active site concentrations and similar acid strengths, but different structures, namely zeolite H-ZSM-5 (microporous channels, diameter ~5.5 Å) and amorphous aluminosilicate (with average pore diameter ~50 Å).

[1] Current address: Department of Chemistry, University of Manchester Institute of Science and Technology, P.O. Box 88, Manchester M60 1QD, U.K.

[2] Current address: Koninklijke/Shell-Laboratorium, Amsterdam P.O. Box 38000, 1030 BN Amsterdam, The Netherlands.

0021-9517/94 $6.00

II. EXPERIMENTAL

2.1. Materials

Four ZSM-5 samples with different crystallite sizes but rather similar acid site concentrations were used in this study. These samples have been described in detail elsewhere (9, 10), but their main characteristics are summarized for convenience in Table 1. The samples were converted into the acid (H^+) form via NH_4^+ ion exchange and calcination at 550°C. Samples 1, 3, and 4 were fully exchanged, while sample 2 had 35% residual sodium ions.

In addition, an amorphous aluminosilicate (AAS) sample (15% Al_2O_3) was used for comparative studies. This sample was described briefly elsewhere (9, 10), but more details are given in the present article. Nitrogen adsorption experiments gave a surface area S_{BET} = 680 $m^2\ g^{-1}$, pore volume of 0.46 $cm^3\ g^{-1}$ (as compared with 0.17 $cm^3\ g^{-1}$ for the ZSM-5 samples), and an average pore diameter of 50 Å. Scanning electron micrographs show the AAS sample to be composed of globules, diameter typically 100 μm. It has Brønsted acid sites (OH groups) with a strength similar to that for the bridging OH groups in the ZSM-5 samples, but a lower concentration (see results and Ref. (10)).

n-Butanol and di-*n*-butyl ether (AR grade) were distilled and stored over a molecular sieve to remove any possible remaining traces of water. All gases were dried over a molecular sieve prior to use. The residual water content was less than 10 ppm.

2.2. GC Kinetic Studies

The dehydration reaction was studied in a flow microreactor with on-line GC product analysis. Full details are given in Ref. (10). Briefly, the reactor was loaded with 0.005–0.05 g of pelletized catalyst (0.3–0.5 mm fraction) and the reactant (*n*-butanol or di-*n*-butyl ether) was fed into the reactor as a gaseous mixture with helium (alcohol concentration typically 0.7 mol%, ether concentration typically 0.8 mol%, overall pressure 1 atm). The gas flow rate was typically 30–40 cm^3/min. The reaction was studied in the temperature range 105–185°C and the conversion was kept to less than 10% (except for special experiments).

TABLE 1

Sample Characterization

Sample	Crystallite size (μm)	$[H^+] \times 10^{20}$ ions/g
1	<0.1	2.3
2	0.5–4	3.3
3	4–6	2.8
4	15–20	2.8

Prior to reaction, the sample was treated for 1 h in a flow of oxygen at 500°C and for 2 h in a helium flow at 450°C. The products were analyzed using two columns:

(1) a polysorb column to separate butene, water, and isomeric alcohols (thermal conductivity detector, 130°C) and to separate butene, isomeric alcohols, and isomeric butyl ethers (FID, 170°C); and

(2) 0.01% disodium disulphophtalocyanine Co(II) on activated carbon (0.25–0.5 mm fraction) to separate the various butene isomers (FID, 60°C).

The rate of formation of products is defined as $W_x(y)$—rate of formation of product x on dehydration of reagent y. Thus, for alcohol dehydration, we have

$$\left.\begin{aligned} W_B(n\text{-BuOH}) &= F[C_4H_8]/m \\ W_{H_2O}(n\text{-BuOH}) &= F[H_2O]/m \\ W_{Bu_2O}(n\text{-BuOH}) &= F[(C_4H_9)_2O]/m \end{aligned}\right\}$$

where B = C_4H_8 and Bu = C_4H_9,

where F is the helium–alcohol flow rate ($cm^3\ s^{-1}$); $[C_4H_8]$, $[H_2O]$, and $[(C_4H_9)_2O]$ are the concentrations of products determined by GC (molecules/cm^3); and m is the sample mass (g).

Corresponding expressions can be defined for the case of ether decomposition:

$$W_B(n\text{-}Bu_2O) = F[C_4H_8]/m, \text{ etc.}$$

The rate at which alcohol or ether is incident on the sample or the rate of exit of unreacted alcohol or ether is determined from

$$V(n\text{-BuOH}) = F[C_4H_9OH]/m, \text{ and}$$

$$V(n\text{-}Bu_2O) = F[(C_4H_9)_2O]/m,$$

respectively.

Experiments with finer pellet fractions gave identical reaction rates, as did experiments with ZSM-5 samples of different crystallite sizes. This shows the absence of diffusion limitations (this refers to both intercrystalline diffusion within pellets and intracrystalline diffusion in the channels of ZSM-5 crystallites) for the reactions studied.

2.3. FTIR Studies

IR studies of acidity and reaction were carried out on a Bruker FTIR spectrometer (IFS-113V), using a thermostatted *in situ* cell. The construction of the FTIR cell was described in more detail in Ref. (10). The zeolite or AAS samples were pressed into self-supporting disks (mass typically 25 mg, ρ = 6–12 mg/cm^2). These were then calcined for 1 h in air and for 2 h in vacuum (10^{-4} Torr) at 450°C, and finally cooled to the desired temperature, at

which point the IR spectrum of the dehydrated sample was recorded for reference purposes. The number of Brønsted acid sites (bridging OH groups) and Lewis acid sites was determined using adsorption of pyridine and carbon monoxide, respectively, as described in Refs. (10, 14, 15). Pyridine was injected in portions of 0.5 μl and the spectra recorded at 150°C. Carbon monoxide was adsorbed in small doses (0.5 cm^3) at a pressure of 50–200 Torr and the spectra recorded at −190°C. By plotting the difference between these recorded spectra and the spectrum of the purely dehydrated sample, the spectrum of the adsorbed species is obtained.

Kinetic studies of the dehydration reaction were carried out in the thermostatted *in situ* IR cell at 100°C. The desired amount of alcohol to acid sites ($[ROH]/[H^+]$ = 0.5 : 1) was injected into the cell containing the previously dehydrated sample and the kinetics of reaction were studied by following changes in the IR spectra with time. In these kinetic studies, spectra (of 10 scans each) could be collected every 25 s or so in the wavenumber interval 4000–1200 cm^{-1} (resolution 4 cm^{-1}). For non-kinetic work a typical number of scans was 200.

III. RESULTS

3.1. Characterization of Acidity

In a previous article we discussed in some detail the use of a number of methods to characterize the concentration of the acid sites in the four ZSM-5 samples (10). These included chemical analysis, pyridine poisoning experiments, infrared studies of adsorbed pyridine and carbon monoxide, and ^1H NMR spectroscopy. Most of the acid sites were shown to be Brønsted sites

$$\begin{array}{c} H^+ \\ | \\ \text{(bridging Al—(OH)—Si groups)} \end{array},$$

but a smaller number of Lewis sites were also present in some samples (amounting to less than 10% of the overall Al content). However, it was shown that it is the Brønsted sites that are active in the dehydration reaction.

The acidity of the amorphous aluminosilicate sample was mentioned briefly in Ref. (10), but here we report IR characterization of its acid properties in more detail so as to compare them with those of the ZSM-5 samples.

3.1.1. Pyridine adsorption (150°C). Typical IR spectra for pyridine adsorbed on ZSM-5 and on AAS are shown in Fig. 1. Quantitative results from these spectra were given in Ref. (10). The two characteristic peaks are the ones at 1545 cm^{-1} (PyH^+) and 1455 cm^{-1}, corresponding to pyridine interacting with Brønsted and Lewis sites, respectively, in accordance with Refs. (14, 15). Other peaks corresponding to PyH^+ are located at 1630 cm^{-1}, 1610 cm^{-1}, and 1490 cm^{-1}. Lines from Pyridine adsorbed on Lewis acid sites are located at 1620 cm^{-1} and 1490 cm^{-1}. Other peaks in the spectra correspond to physisorbed pyridine or pyridine hydrogen-bonded to silanol groups.

In the case of the zeolite, a rather intense pyridinium PyH^+ peak is observed, i.e., a significant number of Brønsted acid sites. However, only a small shoulder is observed at 1455 cm^{-1}, corresponding to a trace amount of Lewis acid sites. On an increase in the amount of pyridine, only peaks corresponding to physisorbed species increase (at 1445 cm^{-1}, Figs. 1a, b), indicating that the Brønsted and Lewis acid sites are already saturated, and hence their intensities can be used to estimate the concentrations of the respective sites.

The results for the AAS sample are shown in Figs. 1c and 1d. Again, once the Brønsted and Lewis sites are occupied (Fig. 1c), increasing the amount of pyridine results in increasing intensities only for peaks arising from physisorbed pyridine or pyridine hydrogen-bonded to silanol groups (e.g., increasing shoulder at 1445 cm^{-1}). Comparing the results with those for the ZSM-5 sample, it is seen that the AAS has a lower Brønsted site concentration and a much more significant Lewis site concentration. As already reported in Ref. (10), the concentration of Brønsted sites for the AAS sample was found to be

$$[H^+] = 1.1 \times 10^{20} \text{ ions/g}.$$

3.1.2. Carbon monoxide adsorption. Carbon monoxide adsorption at low temperature (−190°C) was used to probe the types of acid sites and their strengths. The procedure was described in detail in Ref. (10). Illustrative results are shown for ZSM-5 and AAS samples in Fig. 2.

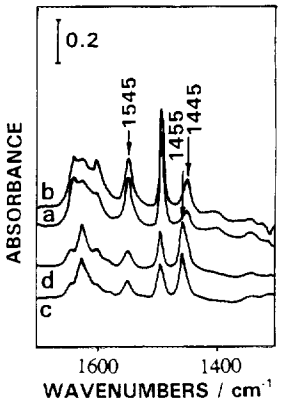

FIG. 1. FTIR difference spectra of adsorbed pyridine on H-ZSM-5 and amorphous aluminosilicate (AAS) at T = 150°C. (a) H-ZSM-5 (sample 2), m = 18.25 mg, ρ = 9.1 mg/cm², 1 μl pyridine; (b) as for (a) + extra 1 μl pyridine; (c) AAS, m = 17.5 mg, ρ = 8.0 mg/cm², 0.5 μl pyridine; (d) as for (c) + extra 0.5 μl pyridine.

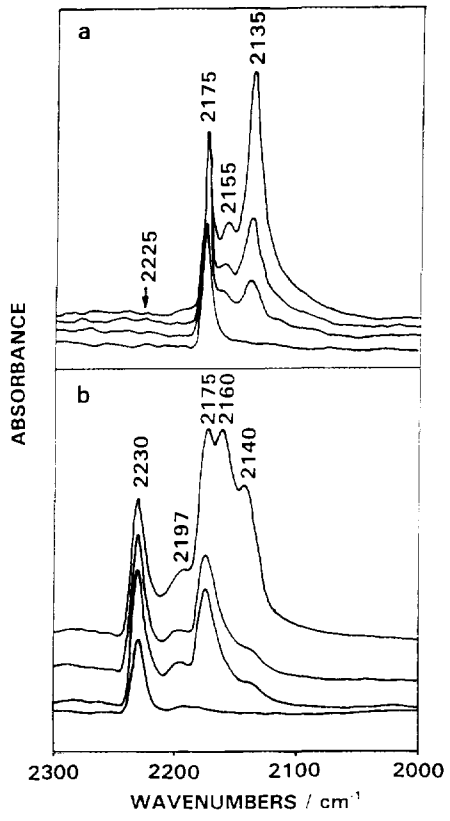

FIG. 2. FTIR difference spectra for carbon monoxide adsorbed on (a) ZSM-5 and (b) AAS, showing C≡O stretching vibration region (T = −190°C), with increasing CO pressure (10^{-2} to 2.10^{-1} Torr).

In the CO stretching region, a peak is observed in all cases at ~2175 cm^{-1}, which is assigned to CO interacting with Brønsted acid sites, in accordance with Ref. (15). Peaks are also observed in the range 2190–2230 cm^{-1}, characteristic of CO adsorbed on Lewis sites of various strengths (15). For the AAS at low CO pressure, an intense peak is observed at 2230 cm^{-1} (strong Lewis sites). The intensity of this peak increases to a maximum as more CO is introduced. The growth of this peak with increasing CO pressure is accompanied by growth of peaks at 2197 cm^{-1} (weak Lewis sites) and 2175 cm^{-1} (Brønsted acid sites). At even higher pressures, peaks at ~2160 cm^{-1} and ~2140 cm^{-1}, characteristic of physisorbed or condensed CO, are observed. For ZSM-5, Lewis acid site peaks are much less intense, and indeed are absent for some samples.

While the numbers of Brønsted acid sites in ZSM-5 and AAS differ, the acid strengths are rather similar. This is illustrated by the results in Fig. 3, where the pertubation in the OH stretching vibration ν_{OH}, as a result of low temperature CO adsorption, is shown. Carbon monoxide interacts with the Brønsted sites by means of hydrogen bonding, which results in a shift of the acid OH stretching vibration to lower wavenumber (15–18). The replacement of the sharp ν_{OH} peaks (at 3615 cm^{-1} and 3740 cm^{-1} for ZSM-5 and AAS, respectively) with broad, intense components at lower wavenumber, as shown in Fig. 3, is typical of such hydrogen bonds. Furthermore, it is known that the shift $\Delta\nu_{OH}$ on hydrogen bonding is proportional to the strength of the Brønsted acid sites (15, 16). For H-ZSM-5, $\Delta\nu_{OH}$ has a value of 300 cm^{-1}, which is in good agreement with the literature (for example, a value of 310 cm^{-1} is given in Ref. (17)). The AAS sample gives a more complicated picture. The broad peak for hydrogen-bonded acid OH groups does not have a well-defined maximum. This reflects the heterogeneity of the acid sites and complicates the determination of $\Delta\nu_{OH}$. A similar picture for AAS was observed in Ref. (18), where the authors conclude that "the broad absorption extending from 3600 cm^{-1} to lower frequencies particularly suggests the existence of OH groups with high hydrogen-bond donor strength which may be considered tentatively as those developing protonic acidity." Taking an average position of this broad band in the range 3600–3280 cm^{-1} as 3440 cm^{-1}, we estimate the average shift $\Delta\nu_{OH}$ for the amorphous aluminosilicate to be 300 cm^{-1}. Thus, we conclude that the average acid strengths of the Brønsted acid sites on the H-ZSM-5 and AAS samples are close, although the AAS has a wider diversity of sites ranging from ones that are weaker than in H-ZSM-5 to ones that are stronger.

The strengths of the Brønsted acid sites in these systems can also be compared using the heat of protonation of a base such as pyridine. Thus, in Ref. (19), the heat of protonation of pyridine on zeolite H-ZSM-5 was found to be 172 kJ/mol, while in Ref. (20) a similar value of 177 kJ/mol was found for amorphous aluminosilicate.

Thus, on the basis of the above discussion, we conclude that the H-ZSM-5 and AAS samples have similar

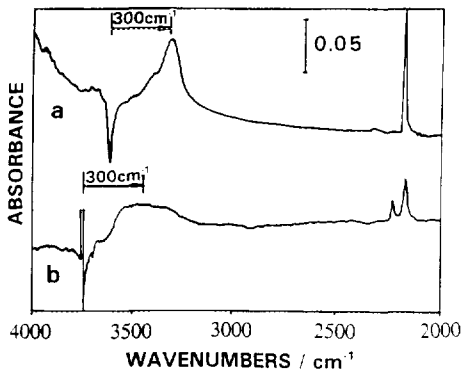

FIG. 3. FTIR difference spectra for carbon monoxide adsorbed on (a) ZSM-5 and (b) AAS, showing OH vibration region as well as C≡O stretching vibration region (T = −190°C).

average acid strengths but different acid site concentration and distribution.

3.2. Reaction on Zeolite H-ZSM-5

3.2.1. GC kinetic study. The kinetics of *n*-butanol dehydration on H-ZSM-5 (sample 1) is shown in Fig. 4. In this experiment, the time necessary to saturate the sample with alcohol is seen to be ~5 min and this saturation corresponds to 8×10^{20} molecules/g of adsorbed alcohol. This value exceeds by 3.5 times the number of bridging OH groups in the zeolite. Thus, under the conditions of our GC experiment, butanol must be present in two forms: (1) hydrogen-bonded to bridging acid OH groups, and (2) "free", i.e., non-bonded to these groups.

However, the time to fill all the zeolite channels with alcohol is not sufficient to obtain steady-state values for W_B and W_{Bu_2O}. The gradual growth of W_{Bu_2O} to a steady-state value in the course of 30 min or so suggests the formation and accumulation of ether inside the zeolite pores, which then gradually desorbs. The concentration of organic product molecules remaining adsorbed in the zeolite channels when reaction is at steady state is given by

$$N = S_{H_2O} - S_{Bu_2O} - S_B,$$

where S_i is the area under the rate of formation curve for product i in Fig. 4. The estimate obtained in this manner has a significantly large value of $\sim 1 \times 10^{20}$ molecules/g_{cat}, which corresponds to approximately half the number of active sites in the catalyst (see Table 1, sample 1). It is known that butene easily oligomerizes on such acid zeolites (9–11). However, this would lead to rapid catalyst deactivation, which is not observed in this initial region. Hence, the adsorbed organic observed here must be mostly ether or its precursor, namely alkoxide, i.e., *n*-butyl silyl ether $\equiv$–O–C_4H_9 (see also Ref. (10)).

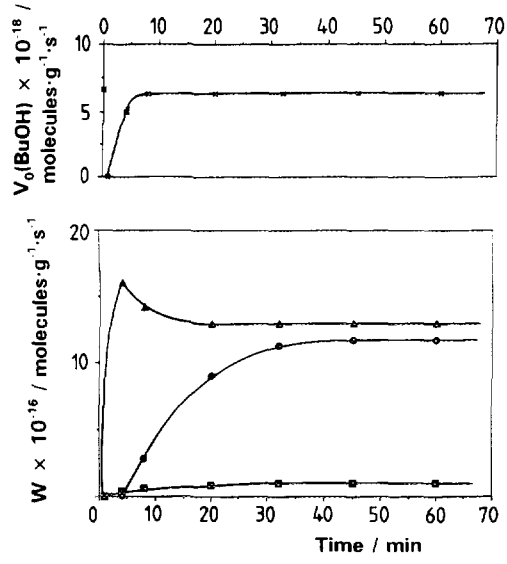

FIG. 4. Kinetics of *n*-butanol dehydration on H-ZSM-5 (microflow reactor, sample 1, m = 0.015 g, T = 130°C): (▲) water, (●) *n*-di-butyl ether, (■) butene, (×) *n*-butanol.

TABLE 2

Extent of Deactivation

Sample	Temperature/°C		
	130	150	165
1	—	—	+
2	—	+	+
4	—	+	+

Note. + denotes significant deactivation (see text for definition).

The retention of ether (or its precursor) in the zeolite channels (as described above) does not arise from diffusion difficulties, since kinetic curves identical to those presented in Fig. 4 are obtained for samples with crystallites of different sizes (samples 1–4) and pellets of different sizes. On a decrease in the reaction temperature, the time necessary to reach steady state increases ($t \approx 50$ min at 110°C), and on an increase in the reaction temperature, the time decreases to $t < 5$ min at 170°C. As the temperature increases, catalyst deactivation in the course of the reaction becomes more noticeable. Deactivation arises from poisoning of the active sites (Brønsted sites) by butene oligomers (as was observed by us in a previous study involving the isobutanol/H-ZSM-5 system (9, 10)). Thus, at these higher temperatures, the functions $W_B(t)$ and $W_{Bu_2O}(t)$ reach a maximum and then fall off with time, rather than reaching a steady state. The ascending part in the initial region of the reaction arises from saturation of the zeolite with alcohol and the retention of product (ether); the descending part is caused by deactivation. And so, as was the case in Ref. (9) for isobutanol, the greatest degree of catalyst deactivation was observed for the samples with large crystallite size and with residual sodium ions. The data obtained are summarised in Table 2. Here the sign + denotes significant deactivation, i.e., the case where the reaction rate decreases by more than 10% of its maximum observed value within 1 h of reaching that maximum rate.

The results in Fig. 5 show the reaction rate constants for samples of different crystallite sizes in the usual Arrhenius coordinates. These constants are determined from $k = W_{max}/N$, where W_{max} is the steady-state or maximum rate (9) of product formation (butene or ether) under the given reaction conditions, and N is the number of

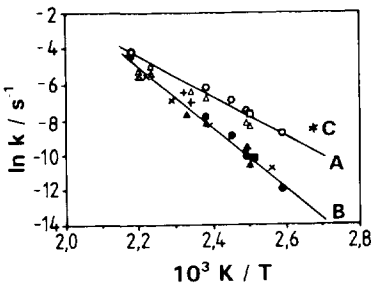

FIG. 5. Arrhenius plots for dehydration of butanol and butyl ether (on ZSM-5 samples of different crystallite sizes). Curve A: dehydration of alcohol to all products (to butene and ether, or which is equivalent, to water) (microflow reactor)—sample 1 (○), sample 2 (△), sample 4 (□). Curve B: dehydration of alcohol or ether to butene only (microflow reactor)—from *n*-BuOH: sample 1 (●), sample 2 (▲), sample 4 (■); from *n*-Bu_2O: sample 1 (×), sample 4 (+). Point C: evolution of water (FTIR kinetic studies). Some points for sample 2 were taken from Ref. (8).

active sites for the given ZSM-5 sample (see Table 1). In principle, there is a danger of obtaining erroneously low values for the rate constants if accumulation of ether in the sample is not yet complete and oligomerization (i.e., poisoning of active sites) has already taken place to a considerable extent. However, this is not a serious complication because we have found that at the given reaction temperatures, when oligomerization is significant, accumulation of ether becomes complete very quickly. For example, in the case of sample 2 at 150°C, W_B and W_{Bu_2O} reach maximum values in 8 min, while for the next 60 min of reaction, the rate decreases by only 15%. An explanation for this effect will be given in the Discussion.

The points lying on line A correspond to total rates of dehydration of butanol:

$$n\text{-}C_4H_9OH \rightarrow C_4H_8 + n\text{-}(C_4H_9)_2O$$

$$k = \frac{W_B + W_{Bu_2O}}{N}.$$

Points lying on line B correspond to rates of dehydration of butanol to butene only.

Identical results for experiments with samples of different crystallite size show the absence of diffusion difficulties in the decomposition of both the alcohol and the ether. The average value for the activation energy of *n*-butanol dehydration (elimination of water) as determined from line A is 22 ± 2 kcal/mol, while that for butene formation alone (from alcohol or ether—line B) is 33 ± 2 kcal/mol. On comparing lines A and B, it is seen that at 110°C, butene makes up only 6% of all organic products of dehydration, while at 180°C, butene already makes up 60%. The obtained difference in activation energies for dehydration of *n*-butanol to all products (22 kcal/mol) and dehydration of *n*-butanol to butene (33 kcal/mol) reflects the change in selectivity of the reaction in favour of butene with increasing temperature.

The above data were obtained in conditions where conversion of alcohol did not exceed 5% (in actual fact, it was usually ~2%). In a special series of experiments, higher conversion was obtained by varying the contact time of the reactants with the catalyst by changing the rate of reactant flow to the reactor ($\tau \propto 1/V_0$) (Fig. 6). Under these conditions, conversion to butene shows a linear dependence on V_0^{-1}, which indicates a constant rate of butene formation for any degree of conversion ($[C_4H_8]/[C_4H_9OH] = W_B \cdot V_0^{-1}$, by definition). As for ether, less ether appears in the reaction products with increasing contact time. This conclusion follows from the nonlinear dependence of conversion to ether on V_0^{-1}, and probably arises from the subsequent decomposition of the ether to butene and alcohol.

When di-*n*-butyl ether was used as the initial reactant, the rate of butene formation was similar to that for its formation from alcohol. At $T \leq 130$°C, W_B reaches a steady state at the same time as the sample becomes saturated in ether. At $T > 130$°C, catalyst deactivation is similar to that described in Table 2. The observed rate constants for butene formation from ether are calculated as described above, and lie on line B (Fig. 5).

3.2.2. FTIR kinetic study. IR spectra of the adsorbed molecules at increasing reaction times at 100°C are shown in Fig. 7. These are difference spectra, from which the spectrum of the original dehydrated H-ZSM-5 before adsorption of alcohol has been subtracted. The first spectrum was recorded 25 s after introduction of alcohol. Detailed assignment of all peaks is not attempted here, but the similarity in peak positions to the spectra of liquid *n*-butanol (21) and *n*-butanol adsorbed on unreactive aerosil enable us to conclude that this first spectrum shows characteristic peaks for adsorbed unreacted *n*-butanol. More

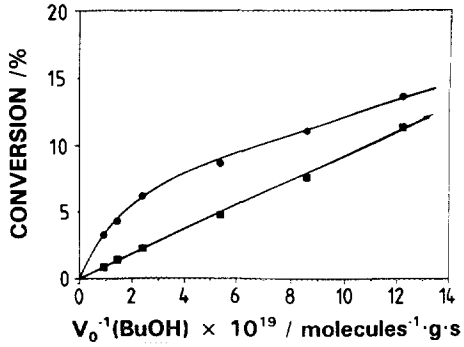

FIG. 6. Dependence of conversion for *n*-butanol dehydration on space velocity: (●) ether, (■) butene. Conversion is defined as W_B/V_0 for conversion to butene and W_{Bu_2O}/V_0 for conversion to ether. See text for more details.

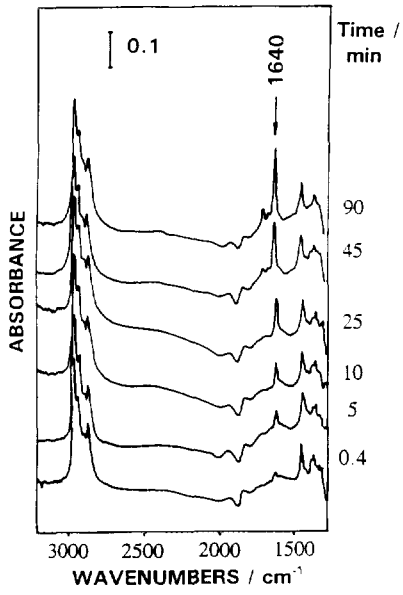

FIG. 7. FTIR difference spectra showing the course of *n*-butanol dehydration on H-ZSM-5 (sample 2) at 100°C as a function of time.

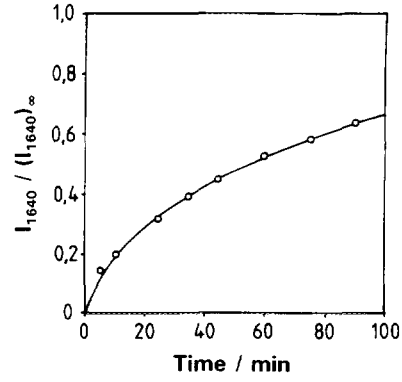

FIG. 8. Kinetics of *n*-butanol dehydration on H-ZSM-5 (sample 2) at 100°C, determined from FTIR data in Fig. 7 for evolution of the 1640 cm^{-1} water peak.

specifically, the peaks at 2965, 2940, 2900, and 2880 cm^{-1} correspond to C–H stretching vibrations, the peak at 1465 cm^{-1} corresponds to deformation vibrations of CH_3 and CH_2 groups, and the peak in the 1380 cm^{-1} region most likely corresponds to deformation vibrations of CH_3 groups (22). The two broad peaks at ~2450 cm^{-1} and ~1600 cm^{-1} correspond to OH groups of zeolite which are hydrogen-bonded to alcohol molecules. We observed rather similar spectra earlier for isobutanol and *tert*-butanol adsorbed on H-ZSM-5 (10, 11).

The main change in the spectra with time is the appearance and growth of the peak at 1640 cm^{-1}, corresponding to deformation vibrations of adsorbed water. This is accompanied by a growth of weak peaks at 1718 cm^{-1} and 1680 cm^{-1}, which we assign to carbonyl group vibrations (22) (the carbonyls forming as a result of butanol dehydrogenation). However, it is known that the extinction coefficients for such C=O vibrations are high (22) and so we suggest that only small quantities of carbonyl species are actually formed in the course of the reaction.

The kinetics of water formation, derived from the data in Fig. 7, is shown in Fig. 8. $(I_{1640})_\infty$ is the maximum intensity of the 1640 cm^{-1} water peak, obtained after heating the sample at higher temperatures (150°C) until no further change occurs (i.e., dehydration is complete) and then cooling it back to reaction temperatures. This intensity corresponds to the total amount of water that can be obtained on decomposition of the adsorbed alcohol molecules. As was the case for isobutanol and *tert*-butanol, $(I_{1640})_\infty/I_{1465} \approx 4$. From the value of $I_{1640}/(I_{1640})_\infty$, it is seen that after 90 min, about 60% dehydration reaction has taken place. The obtained kinetic dependence is an exponential function with a rate constant of 1.7×10^{-4} s^{-1}. This dehydration rate constant obtained from IR data is included in the Arrhenius plot of Fig. 5 as point C.

3.3. Reaction on Amorphous Aluminosilicate (AAS)

For dehydration of *n*-butanol on AAS, butene is the major product over the whole temperature range studied. The time necessary for complete adsorption of alcohol in this experiment is ~7 min, with an alcohol saturation adsorption value of 3.2×10^{20} molecules/g (Fig. 9). The difference between the kinetic curves in Fig. 4 and Fig. 9 is the absence in the case of the AAS of a fast evolution of water that precedes the evolution of organics (B and

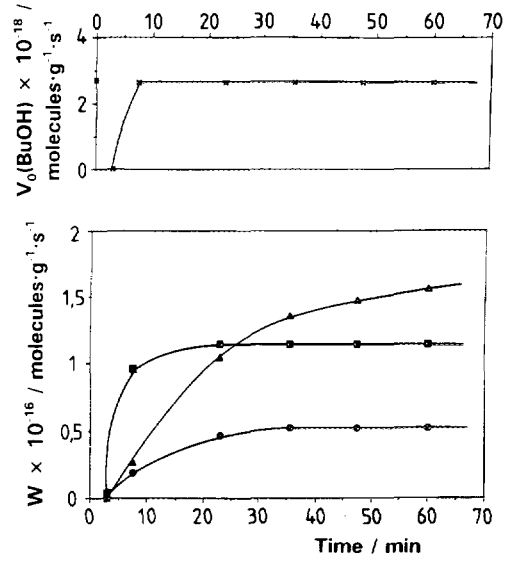

FIG. 9. Kinetics of *n*-butanol dehydration on amorphous aluminosilicate (m = 0.064 g, T = 130°C, microflow reactor): (▲) water, (●) *n*-di-butyl ether, (■) butene, (×) *n*-butanol.

Bu_2O). This may arise from adsorption and hence retention of the so-formed water in ultramicroporous cavities (big enough for water molecules but not for the organic products), which have been suggested to exist in amorphous aluminosilicate samples (23).

The kinetics of reaction when di-*n*-butyl ether is used as the initial reagent is shown in Fig. 10. Here also, one can see a nonsteady-state region of reaction after saturation of the sample with ether ($t_{sat} \approx 3$ min). In this initial region, W_B is higher than its subsequent steady-state value, and the so-formed butanol is presumably retained in the zeolite pores. At steady state, $W_{BuOH} < W_B$, which means that we are not only observing decomposition of ether to butene and alcohol, but also subsequent further dehydration of alcohol to butene and water. Only traces of water were detected in the timescale of the experiments. This again may arise from preferential retention of water molecules in ultramicroporous cavities as described above.

In order to exclude the possibility of the butanol and butyl ether dehydration reactions proceeding on Lewis acid sites, special experiments were carried out in which acetonitrile was preadsorbed on the AAS in excess prior to reaction, so as to poison the Lewis sites. No effect was observed on the kinetics of reaction for alcohol or ether dehydration.

The observed steady-state rate constants are shown in Fig. 11 for the two reactions

$C_4H_9OH \rightarrow C_4H_8 + (C_4H_9)_2O$: $k_B(BuOH)$ and $k_{B+Bu_2O}(BuOH)$

$(C_4H_9)_2O \rightarrow C_4H_8 + C_4H_9OH$: $k_B(Bu_2O)$.

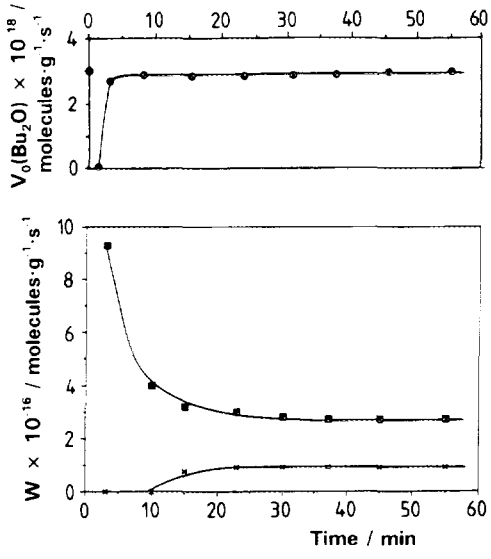

FIG. 10. Kinetics of di-*n*-butyl ether dehydration on amorphous aluminosilicate (m = 0.026 g, T = 130°C, microflow reactor): (■) butene, (×) *n*-butanol, (●) *n*-di-butyl ether.

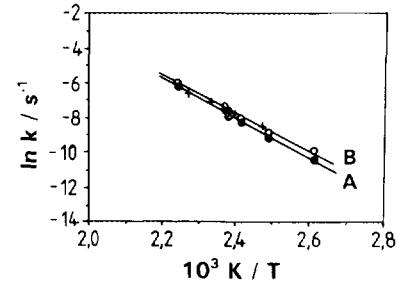

FIG. 11. Arrhenius plots for dehydration of *n*-butanol and *n*-di-butyl ether on amorphous aluminosilicate (microflow reactor). Curve A: dehydration of alcohol or ether to butene; Curve B: dehydration of alcohol to butene and ether. (○) *n*-BuOH → C_4H_8; (+) *n*-Bu_2O → C_4H_8; (●) *n*-BuOH → C_4H_8 + $(C_4H_9)_2O$.

These constants were determined in the same way as described above for the zeolites, from W/N, where W is the steady-state rate of reaction (no deactivation was observed on AAS in the temperature range employed) and N is the number of active sites. The observed rates of formation of butene from alcohol and from ether are seen to be close in value over the temperature range used. The total rates of butanol dehydration (to butene and ether, line B) are also similar, probably because of the preferential selectivity of dehydration on AAS to butene at all the temperatures studied. Thus, for clarity, we have drawn only two lines in Fig. 11. However, considering the three rate constants separately, the following activation energies are obtained: E_B(*n*-BuOH) = 23 ± 2 kcal/mol, E_{B+Bu_2O}(*n*-BuOH) = 22 ± 2 kcal/mol, and E_B(*n*-Bu_2O) = 18 ± 2 kcal/mol.

3.4. Comparison of the Course of Reaction on H-ZSM-5 and AAS

If we compare alcohol dehydration on the ZSM-5 and on AAS, it is seen that the product distribution differs. The main product for ZSM-5 zeolites is di-*n*-butyl ether, while for AAS it is butene (see Figs. 4 and 9). This difference can be conveniently discussed using the function W_B/W_{Bu_2O}, which is plotted in Fig. 12 for both cases. At 130°C, this ratio W_B/W_{Bu_2O} differs by a factor of 25 times for the two types of acid catalyst. Moreover, selectivity changes very sharply with temperature for H-ZSM-5, in contrast to AAS. For example, in the case of ZSM-5, the selectivity to butene changes from 6% (at 105°C) to 60% (at 180°C). On AAS, in the same temperature range, the selectivity to butene changes only from 57 to 80%. This is reflected in the temperature dependence of the function W_B/W_{Bu_2O}. From the data in Fig. 12, then, for H-ZSM-5,

$$W_B/W_{Bu_2O} = \alpha \cdot \exp(-21{,}000/RT),$$

while for AAS,

$$W_B/W_{Bu_2O} = \alpha' \cdot \exp(-6{,}000/RT).$$

On the other hand, the overall rate constants for dehydration to all products (butene and ether) are quite similar in the two cases, being only two to three times higher for the zeolite, and show identical activation energies of 22 kcal/mol (Figs. 5 and 11). This difference of two to three times (which remains constant with temperature) may be due either to an error in the determination of the number of active sites (which we think unlikely, but cannot exclude), or to a slightly higher activity of the acid OH groups on ZSM-5 as compared with those on AAS. Indeed, the IR spectra in Fig. 3 suggest that AAS is more heterogeneous, with some sites of both higher and lower acidity present. Nevertheless, we feel that the results for such different samples as H-ZSM-5 and AAS are in fact in quite good agreement.

3.5. Isomeric Distribution of Reaction Products

3.5.1. Butenes. The isomeric distribution formed on decomposition of alcohol and ether on zeolites of different crystallite sizes, and also on the AAS, are presented in Table 3. On dehydration of alcohol on ZSM-5 sample 1 (smallest crystallites), the major product is but-1-ene. With increasing crystallite size, the butene distribution shifts towards (although it does not completely reach) the equilibrium distribution. The distribution closest to equilibrium was found on sample 2 (containing residual sodium ions). Comparing the results for alcohol and ether decomposition, one can see that although ether gives a slightly different distribution of butenes for each sample, nevertheless, the dependence on crystallite size, etc., follows the same trend as that observed for alcohol dehydration.

Butenes formed from decomposition of either alcohol or ether on AAS are also close in composition. However,

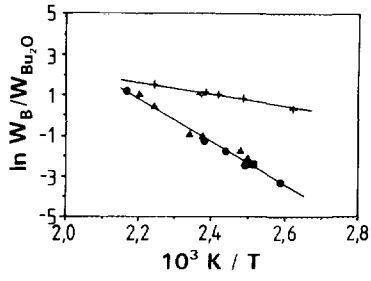

FIG. 12. Arrhenius plot for the ratio of butene and ether formation rates, W_B/W_{Bu_2O}, on alcohol dehydration on H-ZSM-5 and amorphous aluminosilicate (AAS): (●) ZSM-5 sample 1, (▲) ZSM-5 sample 2, (■) ZSM-5 sample 4, (+) AAS.

TABLE 3

Isomeric Distribution of Butenes at 150°C

	Reactant					
	n-BuOH			*n*-Bu_2O		
Sample	1	t-2	c-2	1	t-2	c-2
1	58.0	23.6	18.4	44.0	34.5	21.5
3	55.0	25.5	19.5	—	—	—
4	36.7	41.0	22.4	27.6	51.0	21.4
2	20.1	53.2	26.8	13.5	71.4	15.1
AAS[a]	38.6	31.5	29.9	31.7	35.1	33.2
AAS[b]	—	—	—	17.3	53.0	29.7
Equilibrium[c]	9.3	60.9	29.8	9.3	60.9	29.8

[a] For steady state.
[b] For initial rate of butene formation (Fig. 10 t = 3 min).
[c] From Ref. (26).

while for zeolites the distribution has characteristic maxima—but-1-ene for small crystallites and but-2-ene for large ones—the AAS gives a butene distribution with approximately 33% each of but-1-ene and *cis*- and *trans*-but-2-ene.

All the data included in Table 3 (with one exception) were obtained at 150°C under conditions either of steady state or the maximum rate (for zeolites, when there is some deactivation). When the temperature is changed in the range employed (105–185°C), the isomeric distribution of butenes hardly changes. The one exception to steady-state measurement is the one denoted by (b) in Table 3. Here, the butene distribution is taken from the initial non-steady-state region (of Fig. 10) at the point of maximum rate of butene formation (t = 3 min). As can be seen, this strongly differs from that obtained at steady state and is closer to the equilibrium distribution.

3.5.2. Ethers. As concerns the ether formed on alcohol dehydration, only di-*n*-butyl ether is observed at 130°C. With increasing temperature, traces of the mixed *n,sec*-butyl ether are detected (no more than 5% at 180°C). Isomeric ethers form to a greater extent on samples 2 and 4 than on sample 1 and 3. Thus, on sample 3, the mixed ether makes up 2% of all ether at 150°C, while for sample 1, the same percentage is reached only at 180°C. In contrast to steady-state (or maximum rate) measurements, samples taken in the initial region (t < 10 min) before saturation by reactant alcohol show a much higher relative concentration of the mixed ether. Thus, in this initial region, 32% of the ether formed is the mixed *n,sec*-butyl ether on sample 1 at 180°C. Isomeric ethers were not observed on the AAS sample.

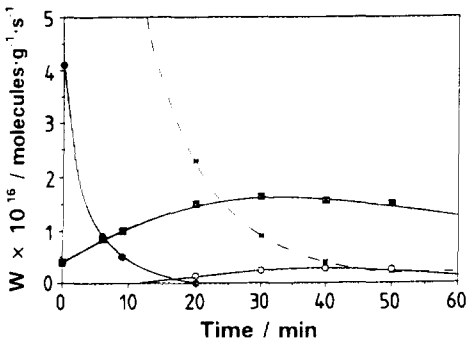

FIG. 13. Purging in H-ZSM-5 after steady-state reaction at 125°C: (×) *n*-BuOH, (●) *n*-Bu_2O, (■) C_4H_8, (○) *n*,*sec*-Bu_2O.

3.6. Non-steady-state Experiments (Purging)

On cessation of the flow of alcohol to the sample after steady state, was reached, the so-called "stop effect" was observed, where the rate of formation of butene after replacement of the alcohol–helium flow with a flow of pure helium was higher than that observed at steady state. The "stop effect" is observed for reactions both on the ZSM-5 zeolites and on the AAS sample (see Figs. 13 and 14), although the effect is significantly larger on zeolites. Thus, at 125°C, the maximum relative increase in W_B(BuOH) or MRI (maximum rate on purging/steady-state rate) after stopping the alcohol feed equals 4.1 for ZSM-5 (Fig. 13) and only 1.3 for AAS (Fig. 14). As concerns the di-*n*-butyl ether product, after cessation of the flow of alcohol, the rate of ether formation falls sharply with no increase. In the case of the zeolite samples, one subsequently observes some formation of *n*,*sec*-butyl ether (Fig. 13). Isomeric ethers are not observed for AAS.

With increasing reaction temperature, the magnitude of the stop effect decreases. At 150°C, the MRI for butene is 2.0 for ZSM-5 (Fig. 15a) and 1.1. for AAS (Fig. 16). In the same way as at lower temperatures, the rate of formation of di-*n*-butyl ether falls sharply at the onset of purging. As concerns butene formation, the tail of the curve after passage through the maximum (Figs. 15a and 16) is described by an exponential. This gives a rate constant for butene formation during the purge of 5.6×10^{-4} s^{-1} for AAS (Fig. 16), which is in good agreement with the rate constant of 5.1×10^{-4} s^{-1} for total dehydration to all products (butene and ether) at steady state. Similarly for ZSM-5, both rate constants are identical (1.1×10^{-3} s^{-1}). For the zeolites, one can observe several "waves" of product formation, some of which were not observed under steady-state conditions (di-*sec*-butyl ether, *sec*-butanol). The "waves" are shifted in time with respect to one another. The same information as in Fig. 15a is presented in Figs. 15b and 15c, but with an expanded *y*-axis, to show the growth of products more clearly. As can be seen, the next product after butene is *n*,*sec*-butyl ether, with a maximum at $t \approx 15$ min (Fig. 15b, MRI = 3.6). The next in intensity is *sec*-butanol and a weaker "wave" of di-*sec*-butyl ether, both with maxima at $t \approx 45$ min (Fig. 15c). On the AAS sample, such a complex collection of products were not observed and the stop effect is confined to an increase only in the rate of butene evolution.

Calculating the amount of product desorbing from the catalyst during the stop effect gives for ZSM-5 (sample 2) 2.95×10^{20} molecules/g_{cat} (80% C_4H_8, 11.9% *n*-Bu_2O, 8.1% *n*,*sec*-Bu_2O, the rest being *sec*-butanol and di-*sec*-butyl ether, Fig. 15a) and for AAS 0.95×10^{20} molecules/g_{cat} (98.5% C_4H_8, 1.5% *n*-Bu_2O, Fig. 16). Comparing these values with the concentration of active sites for these samples, we can see that the number of molecules desorbing from both catalysts practically coincides with the number of their active sites.

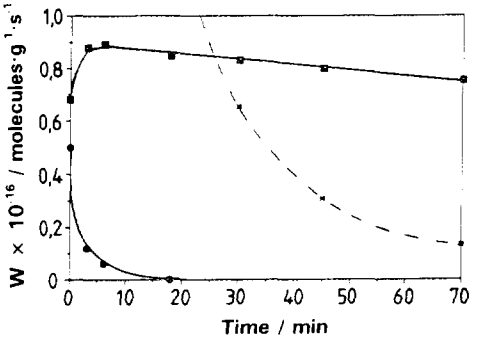

FIG. 14. Purging in amorphous aluminosilicate after steady-state reaction at 125°C: (×) *n*-BuOH, (●) *n*-Bu_2O, (■) C_4H_8.

IV. DISCUSSION

4.1. Mechanism of Decomposition of *n*-BuOH and *n*-Bu_2O on H-ZSM-5 and AAS

In our previous article (10), we substantiated the mechanism of isobutanol dehydration of H-ZSM-5. We suggest that dehydration of *n*-butanol on H-ZSM-5 and amorphous aluminosilicate (AAS) catalysts is described by the same reaction scheme. In the present article we merely draw the scheme in Fig. 17 (while full details may be consulted in Ref. (10)). Let us consider how the data obtained in this paper agree with our proposed scheme.

Case 1. Flow Reactor (GC Kinetic Studies, H-ZSM-5 and AAS)

Let us note immediately that under the flow conditions used here to study reaction, equilibria I and VII are

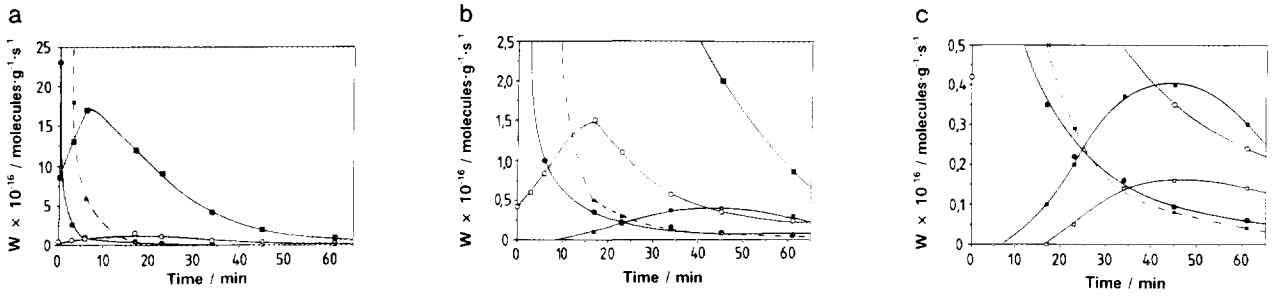

FIG. 15. Purging in H-ZSM-5 after steady-state reaction at 150°C (at various expanded scales): (×) *n*-BuOH, (●) *n*-Bu_2O, (■) C_4H_8, (○) *n*,*sec*-Bu_2O, (⊞) *sec*-BuOH, (□) *sec*,*sec*-Bu_2O.

shifted in the direction of the adsorbed complexes (we observed zero orders of reaction with respect to alcohol and ether) and equilibrium II is shifted to the right (absence of butanol isomers in the reaction products, in contrast to isomers of other species, i.e., butene and butyl ether isomers, which are also in equilibrium with the ≡–O–C_4H_9 alkoxide intermediate). Pathway VI—oligomerization of the products on the active centres—is not considered here, since experimental conditions were such as to reduce oligomerization to a minimum.

In the GC kinetic studies, the following tendencies were observed:

1. In the initial stages of reaction, accumulation of reaction product in the sample is observed: accumulation of ether (or its precursor ≡–O–C_4H_9) when the reactant is alcohol (Fig. 4 for H-ZSM-5 and Fig. 9 for AAS) or alcohol accumulation when the reactant is ether (Fig. 10 for AAS).

2. Under steady-state conditions, butene is formed with the same rate both from alcohol and from ether (Fig. 5 for H-ZSM-5, Fig. 11 for AAS).

3. Butenes forming either from alcohol or from ether on one and the same sample have qualitatively similar isomeric distributions. For both reactants, the same tendencies in butene isomer distribution are observed on going from one sample to the next (Table 3).

4. With increasing degree of alcohol conversion, the rate of butene formation remains constant, while the rate of ether formation decreases (Fig. 6 for H-ZSM-5).

These tendencies indicate that the steady-state concentration of active sites covered with adsorbed alcohol, ether, or butene (as ≡–O*R*), N_A, N_E, N_B, respectively (where $N_A + N_E + N_B = N$, and N is the total number of active sites in the catalyst), does not depend on the reactant (be it alcohol or ether). Indeed, according to our scheme, the reversible transformation of the alcohol–ether pair,

$$ROH \underset{\text{path III + II or IV}}{\overset{\text{path II + III}}{\rightleftharpoons}} R_2O$$

makes the choice of a particular reactant (alcohol or ether) unimportant. (For path IV, butene is formed simultaneously with alcohol upon decomposition of ether). In both cases, the steady-state rate of butene formation is given by

$$W_B = k_{+5} N_B .$$

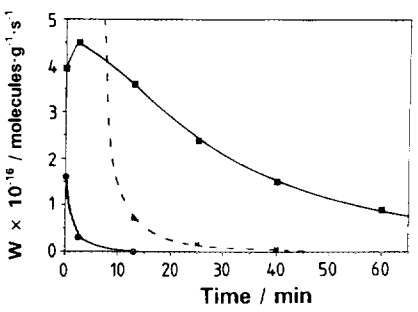

FIG. 16. Purging in amorphous aluminosilicate after steady-state reaction at 150°C: (×) *n*-BuOH, (●) *n*-Bu_2O, (■) C_4H_8.

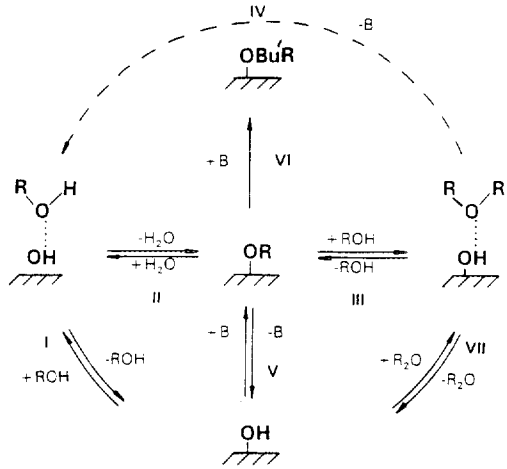

FIG. 17. Reaction scheme for *n*-butanol dehydration (R = C_4H_9, B = C_4H_8 and Bu′ = C_4H_8 group in oligomer). All molecules accompanying the arrows are physisorbed.

It is interesting that in the case of high conversion (non-differential reactor), the reactant feed should change from layer to layer through the catalyst. Thus, if the initial reactant feed is alcohol, then the first layers of catalyst obtain mainly alcohol, while the final layers receive mainly ether (product of dehydration). Simply speaking, the ether formed on the first layers of catalyst decomposes on later layers. Note, however, that the rate of butene formation does not depend on the feed composition and will not change. It is exactly this that we observe in Section 3.2.1, where on increasing degrees of conversion, the rate of butene remains constant, but the rate of ether formation decreases.

Case 2. Static Reactor (FTIR Kinetic Studies, H-ZSM-5)

In the FTIR experiments, the sequence of events can be described as follows:

1. Adsorption of alcohol via path I—which was observed immediately after introduction of alcohol into the reactor. The fact that the intensities of the peaks corresponding to CH_2 and CH_3 vibrations reached their maximum values in less than 25 s after the start of the experiment (the time required to record the first IR spectrum) shows that adsorption of alcohol onto zeolite is rapid and does not control the kinetics of dehydration.

2. Dehydration of alcohol via path II—which was observed by the appearance and growth in intensity of the peak at 1640 cm^{-1} (corresponding to the deformation vibrations of water molecules).

But what happens to the hydrocarbon fragment of the alcohol molecule? There exist at least four possibilities for interpreting the course of reaction:

a. stopping of reaction at the ≡Si–O*R* intermediate,
b. formation of butene via pathway V, followed by its retention in or desorption from the sample,
c. formation of ether via pathway III, or
d. formation of oligomers via pathway VI.

Possibilities b and c can be rejected immediately. Rejection of possibility b of formation of butene and its retention in the sample is supported by the fact that no peak in the region above 3000 cm^{-1} (characteristic of the C–H vibration in olefins (22)) was observed in the spectra. Note also that the intensities of the peaks for CH_2 and CH_3 vibrations do not change with time; i.e., desorption of organic molecules from the sample does not take place. Thus, the possibility of butene formation followed by its subsequent desorption can also be rejected. The formation of ether (possibility c) is rejected because the kinetic curves for water evolution are seen to tend towards 100% water formation, i.e., to form the equivalent of 1 H_2O molecule from 1 butanol molecule (while for ether formation, one would have expected 0.5 H_2O per butanol molecule.

Thus, possibilities a and d remain. On the basis of our FTIR data, it is not possible to distinguish unabiguously between these two. The changes in the peaks for the CH_2 and CH_3 groups in the course of dehydration are too small to be interpreted. Note that the chance of oligomerization is greater in the FTIR experiments than in the GC studies due to two reasons. First, in the CG experiments, a flow reactor is used and butene is continually pushed out of the reaction zone by butanol molecules, while in the FTIR experiments, the IR cell is a static reactor in which the product accumulates. Second, in the GC experiments, reaction takes place with an excess of alcohol in the zeolite channels (vide supra). This facilitates the formation of ether (path III) from the same intermediate ≡Si–O*R*, and thus hinders the formation of oligomers.

If excess alcohol is used in order to reduce oligomerization in the case of the FTIR studies, then any changes in the IR spectra will be obscured by intense peaks from adsorbed, unreacted alcohol molecules. Moreover, in the case of excess alcohol, it is not even possible to follow the kinetics of reaction (by observing the growth of the water deformation peak at 1640 cm^{-1} with time) because as we have observed, the water molecules formed are immediately displaced from the sample into the gas phase by the excess alcohol molecules adsorbed in the zeolite channels.

Thus, for *n*-butanol dehydration on H-ZSM-5 at a given temperature (100°C), one can see how with differing chemical environments in the zeolite pores, different paths of reaction become prevailing. Under conditions of excess alcohol molecules in the vicinity of the ≡Si–OR intermediate (GC steady-state kinetic studies), equilibrium III is shifted to the right, since there is an excess of reactant (butanol) for ether formation. And the main reaction product under these conditions is ether (ca. 95%). Under conditions where excess alcohol is absent (adsorption of 0.5 ROH : 1H^+, FTIR kinetic studies), and there is no physically adsorbed alcohol in the zeolite channels, path III for the transformation of the intermediate to ether is insignificant. As a result, reaction ends either at ≡Si–OR, at oligomers ≡Si–OBu'R, or at a mixture of both.

The next questions to consider are why the zeolite produces so much more ether than the AAS, and why the selectivity changes so sharply with temperature for H-ZSM-5 (W_B/W_{Bu_2O} has an exponent of −21 kcal/mol—see Section 3.4), but not for AAS (W_B/W_{Bu_2O} has an exponent of −6 kcal/mol). Again, this is most likely explained by a shift of the equilibrium reaction in the zeolite to the right (Fig. 17), i.e., to ether formation. As we have shown above, the rate, W_3 of the reaction between ≡Si–O*R* and *R*OH, which is responsible for this shift, must depend on the alcohol concentration in the vicinity of the active ≡Si–

OR. The higher the alcohol concentration, the more ether forms. One can estimate the alcohol concentration for both the zeolite and AAS. As discussed in Sections 3.2 and 3.3, ZSM-5 adsorbed $\sim 8 \times 10^{20}$ butanol molecules/g, while AAS adsorbs $\sim 3 \times 10^{20}$ molecules/g at 125°C (Figs. 4, 9). Using the pore volumes determined from nitrogen adsorption (see Experimental), we obtain the concentration of adsorbed alcohol for ZSM-5 and AAS of 3.7×10^{21} molecules/cm^3 and 6.5×10^{20} molecules/cm^3, respectively. For comparison, note that liquid *n*-butanol at 25°C contains 6.6×10^{21} molecules/cm^3. Thus, while the density of reactant inside the zeolite is close to that of the liquid, the AAS is more or less empty. This high alcohol concentration in the ZSM-5 explains the higher degree of ether formation inside the zeolite channels. Presumably, as the temperature is increased, less alcohol will remain adsorbed. This will be much more significant for ZSM-5 than for AAS (which is almost empty even at 125°C), and hence results in a significant change of selectivity in favour of butene. However, it is not clear whether the experimentally determined value of this lowering, 15 kcal/mol (21–6 kcal/mol, see Section 3.4) arises purely from a concentration effect (microcapillary condensation of alcohol) or has also a contribution from ether stabilization in zeolite pores.

Analysis of literature data (1, 2, 5, 6, 24) shows that the consecutive-parallel scheme of reaction proposed earlier by Knözinger *et al.* for alcohol dehydration on alumina is still the most widely used scheme to explain the mechanism of alcohol dehydration on acid catalysts:

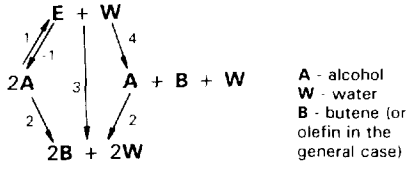

It should be noted that the difference between our "cross" scheme and the scheme proposed by Knözinger *et al.* (1, 2) is rather significant, despite their apparent similarity at first glance. Including an active intermediate ≡–OR at the centre of the scheme enables us not only to explain the change in the reaction paths depending on the environment in the zeolite channels (which was observed in the current work), but also to explain observations of other workers. For example, in studies of the dehydration of ethanol (24) and *n*-butanol (5) on alumina, identical types of dependences were observed for the rate of formation of ether or olefin on alcohol pressures for the two alcohols. However, for any one alcohol, the olefin and ether dependences on alcohol pressure differ considerably. Thus, while the rate of ether formation has an asymptotic dependence on alcohol pressure, reaching a plateau, a dependence which might somehow be described by a Langmuir equation, the rate of formation of olefin has a maximum in the low pressure region and then gradually decreases with pressure. Considering alcohol dehydration to olefin as an independent process (independent of ether formation) led the authors in (24) to suggest two olefin-forming processes on different types of sites. The authors of (5) used a trail-and-error procedure to obtain a best fit function with a maximum, but having no physical meaning. However, starting from our "cross" scheme, it becomes clear that the ascending part of the curve for the rate of olefin formation is related to Langmuir adsorption of alcohol, while on further increase in the alcohol pressure in the zeolite, the formation of ether from the intermediate becomes more favoured and so the rate of butene formation decreases.

It should be noted that the concept of ether and olefin formation via one and the same intermediate was previously proposed by Jacobs *et al.* (25). However, the work was carried out on alcohol dehydration over alkali cation forms of X and Y zeolites, where the nature and origin of the active acid sites was not that clear. This may explain why this proposal was not widely adopted by subsequent workers.

4.2. Physical Meaning of Rate Constants

Let us now on the basis of the proposed reaction scheme consider the physical meaning of the rate constants obtained in the present work.

(a) The rate constants of complete dehydration of alcohol on H-ZSM-5 and AAS, $k = k_B + k_{Bu_2O}$ (GC kinetic studies, line A, Figs. 5 and 11), are obviously effective rate constants, equal to $k_2 \cdot \Theta_A$, where k_2 is the real rate constant of dehydration via path II, and $\Theta_A = N_A/N$ is the steady-state coverage of the active centres by alcohol. Note that only a part of all the active centres are covered with alcohol under steady-state conditions, namely

$$\Theta_A = 1 - \Theta_B - \Theta_E < 1.$$

An obvious consequence of this is that the dehydration rate constants k obtained in this manner are smaller than the true rate constant of dehydration (k_2), and consequently the activation energy (22 kcal/mol for H-ZSM-5 and AAS) has an effective value.

(b) The rate constants for butene formation on H-ZSM-5 and AAS, k_B (GC kinetic studies, line B, Figs. 5 and 11) are also effective constants. They can be considered as alcohol dehydration constants multiplied by selectivity for butene formation $k_2 \cdot \Theta_A \cdot S_B$. As a result, the effective activation energy for dehydration (33 kcal/mol for H-ZSM-5 and 23 kcal/mol for AAS) will include not only the

activation energy for dehydration (22 kcal/mol), but also a term reflecting the change in selectivity of reaction with change of temperature, which in principle is related to the relative "resistance" of the two paths of reaction after elimination of water, namely butene formation and ether formation. For H-ZSM-5 a sharp change in selectivity is observed with change of temperature, and so the extra term in the activation energy, 11 kcal/mol (33–22 kcal/mol) is considerably higher than that for AAS, 1 kcal/mol (23–22 kcal/mol).

Strictly speaking, the dependence of k_B and $k_B + k_{Bu_2O}$ on $1/T$ should not necessarily be exponential. Only the temperature dependence of the ratio of rates of formation of products of the two parallel reactions can be described by an exponential dependence. For example, for H-ZSM-5 (Section 3.4),

$$W_B/W_{Bu_2O} = \alpha \cdot \exp(-21000/RT).$$

However, apparently a temperature interval of 80°C (as was used in our experiments) is narrow enough to allow for a simple exponential approximations for both values, giving effective activation energies rather than true.

(c) The rate constant for alcohol dehydration on H-ZSM-5 (FTIR kinetic studies, Fig. 5, point C) is most likely the real constant of *n*-butanol dehydration for step II, because it is indeed in this step that the elimination of water takes place—a process that we follow in the IR experiments.

Comparing the alcohol dehydration rate constants obtained by the two different methods under completely different conditions (Fig. 5: line A—steady-state GC kinetic study, flow reactor; point C—FTIR kinetic study, static reactor), it can be said that they are rather close in value and differ roughly by no more than three times. This means that under steady-state reaction conditions even at 100°C, a third or more of the active centres of the zeolite will be covered by adsorbed alcohol, which is dehydrated. It is also possible to say that the reaction intermediate ≡Si–O*R* under flow reaction conditions easily transforms to products—ether and butene. If it were not so, the reaction rate constant determined from FTIR data should be considerably higher than the rate constant from GC steady-state data, since all the active centres would be blocked by stable surface species.

Thus, the rate constant for *n*-butanol dehydration determined from GC steady-state data is close in value to the true dehydration rate constant.

4.3. Nature of Reaction Intermediate

Just as was the case in our previous work on isobutanol dehydration on H-ZSM-5 (10), in the FTIR spectra on dehydration of *n*-butanol, the growth of the peak at 1640 cm^{-1} (corresponding to deformation vibration of water) was not accompanied by any significant changes in the peaks corresponding to vibration of CH_2 and CH_3 groups. Note that if under the conditions of our FTIR experiments, the ≡Si–O*R* intermediate is formed (either alone or mixed with oligomer ≡Si–OBu'R), then its IR spectrum should coincide with the spectra for the hydrocarbon skeletons of the alcohol molecules. Thus, it should be said that FTIR is not the best physical method to directly observe the intermediate of this reaction.

Although we have not been able to observe the ≡Si–O*R* intermediate directly, it is nevertheless possible to conclude from the results on the isomeric composition of the reaction products that this intermediate is most likely to be a primary alkoxide (and not a carbonium ion), which on decomposing gives but-1-ene. We observe the preferential formation of but-1-ene for sample 1, with the smallest crystallites. With increasing crystallite size of the zeolite sample, the composition of the butene formed on reaction is shifted more to equilibrium (see Table 3). This clearly suggests secondary isomerization of butene in the zeolite channels; i.e., isomerization of the so-formed butene takes place via step V. However, one should bear in mind that if the decomposition of the ether takes place via a different intermediate than its formation (path IV, elimination of butene without formation of alkoxide), then this butene forming from the ether may be already isomerized; i.e., there may exist yet another route for butene isomerization (step IV) in addition to step V.

As concerns the isomeric composition of butene on alcohol and ether dehydration on AAS, at present it is not completely understood, although it should be noted that this composition is typical for such systems and has been observed earlier (26).

4.4. Explanation of the Stop Effect

A further phenomenon that requires explanation is the so-called "stop effect." This effect was previously observed in alcohol dehydration reactions and deamination reactions on alumina (27, 28). Two explanations have been proposed. For deamination, it was suggested that the amine molecule requires two neighbouring centres in order to react—an acid–base pair. During steady state, it is proposed that acid and base sites of the pair have adsorbed amines, but that on purging, the basic centres are rapidly freed, allowing an amine on a neighbouring acid site to react on the two centres, giving increased reaction rate (27).

The same authors suggest a second explanation for the same stop effect in alcohol dehydration, namely that the extra olefin on purging comes from a stored source of

alcohol species strongly adsorbed on Lewis sites, probably as surface alkoxide. These are presumed to be unreactive to olefin formation but to convert to reactive species on acid OH groups. Similarly, Moravek *et al.* (28) equate the stop effect for alcohol dehydration to a high coverage of surface alkoxides. However, in both cases no satisfactory explanation is given as to why the surface alkoxides that are considered unreactive during steady state become so much more active during purging. Furthermore, the fact that the stop effect takes place in cases where the bimolecular ether product is formed in addition to olefin in the steady-state regime was not taken into account in any of these articles. From the consideration of molecular conversion on the catalyst surface discussed above, it is clear that stopping the alcohol reactant feed results in a very sharp decrease in the rate of ether formation via step III. It means that this route of reaction is closed and all the product of reaction becomes formed via step V. In this situation, butene indeed must be formed at a higher rate than that observed at steady state.

Indeed, we have found that the effective rate constants for the dehydration reaction (to all products) during steady state and for the formation of butene on the descending part of the stop-effect curve practically coincide (Section 3.6) for reactions on both ZSM-5 and AAS. We observed also that the magnitude of the MRI (maximum relative increase of rate) characterising the stop effect correlates with ether formation—the higher the rate of ether formation at steady state, the greater the MRI for butene formation obtained on purging. When the reaction temperature is decreased, the selectivity changes in favour of ether and the MRI increases. For a given temperature, the ZSM-5 produces more ether than does AAS (higher selectivity to ether) and its MRI is higher. Thus, we suggest that the reaction scheme in Fig. 17 is able to explain all the experimental results.

Product peaks subsequent to that of butene during purging reflect processes taking place in the zeolite channels at low coverage. With plenty of free active sites, the butene begins to isomerize freely, resulting in preferential formation of but-2-ene. This then gives rise to subsequent desorption peaks for *n*,*sec*-butyl ether and a less intense peak for *sec*-butanol. The least intense peak observed at the end is di-*sec*-butyl ether, which is formed from interaction of the secondary products—but-2-ene and *sec*-butanol. This shows clearly how in a zeolite a whole series of conversions/reactions can take place. This possibility during the period of purging is related to an increase in the contact time of the molecules with the active centres of the catalyst as they travel through the microporous channels. On the amorphous aluminosilicate sample no new products were observed during purging, presumably because the absence of such a pore confinement as is present in the microporous zeolites means that contact time is not increased, or is increased to a lesser extent in this more open system.

V. CONCLUSIONS

In the present work we have confirmed for *n*-butanol dehydration on H-ZSM-5, and on amorphous aluminosilicate the "cross" scheme for dehydration that was proposed by us earlier for the case of isobutanol (10). According to this scheme, in contrast to the well-known scheme of Knözinger *et al.* (1, 2), the formation of butene and ether products takes place via one and the same intermediate—a highly reactive surface alkoxide species $\equiv$–O–C_4H_9. Furthermore, the rate constant for subsequent formation of ether depends on the concentration of alcohol in the surrounding neighbourhood of the alkoxide (Eley-Ridel mechanism). Stopping the alcohol flow to the reactor (and replacing it by a flow of pure helium) results in a redistribution of the products among the reaction routes, producing a fast fall in the rate of ether formation and an increase in the rate of butene formation (stop effect). Since a similar effect was observed earlier for other reactions with two types of products (intra- and intermolecular elimination) on different aluminosilicate catalysts (although the effect was not satisfactorily explained), we consider that the proposed scheme is perhaps suitable for a wider class of reactions on aluminosilicate catalysts.

As concerns the influence of the microporous structure of the zeolite, a study of the *n*-butanol dehydration reaction on a series of zeolites with similar concentrations of active sites but different crystallite sizes (ranging from <0.1 to 20 μm) has shown that diffusion problems are absent both for reactant and product molecules. Increasing the crystallite size merely results in increasing secondary isomerization of the but-1-ene primary product.

However, in contrast to reaction on an open surface (amorphous aluminosilicate with pore diameter ~50 Å) in the microporous system the concentration of adsorbed reactant is increased, which gives a higher rate of ether formation. The concentration factor gives a decrease in the effective energetic barrier for ether formation on zeolite in comparison with AAS. At low reactant concentration (and consequently, high concentration of free active sites in the catalyst pores), a whole series of subsequent molecular conversions can take place inside the zeolite pores, right up to the formation of di-*sec*-butyl ether from the original *n*-butanol.

ACKNOWLEDGMENTS

We thank Dr. M. Bredikhin for assistance with the low temperature FTIR work. One of us (C.W.) thanks the Royal Society, USSR Academy of Sciences, and the SERC for financial support.

REFERENCES

1. (a) Knozinger, H. *in* "The Chemistry of the Hydroxyl Group" (S. Patai, Ed.), p. 642. Interscience, London, 1971; (b) Knözinger, H., *Angew. Chem. Int. Ed. Engl.* **7,** 791 (1968).
2. Knözinger, H., and Kohne, R., *J. Catal.* **5,** 264 (1966).
3. Chang, C. D., *Catal. Rev. Sci. Eng.* **25,** 1 (1983).
4. Krampera, F., and Beranek, L., *Collect. Czech. Chem. Commun.* **51,** 774 (1986).
5. (a) Yue, P. L., and Olaofe, O., *Chem. Eng. Res. Dev.* **62,** 81 (1984); (b) Yue, P. L., and Olaofe, O., *Chem. Eng. Res. Dev.* **62,** 167 (1984).
6. (a) Aronson, M. T., Gorte, R. J., and Farneth, W. E., *J. Catal.* **105,** 455 (1987); (b) Aronson, M. T., Gorte, R. J., and Farneth, W. E., *J. Catal.* **98,** 434 (1986).
7. Kalvachev, Yu, Bezouhanova, C., and Lechert, H., *Zeolites* **11,** 73 (1991).
8. Makarova, M. A., Williams, C., Thomas, J. M., and Zamaraev, K. I., *Catal. Lett.* **4,** 261 (1990).
9. Makarova, M. A., Williams, C., Romannikov, V. N., Zamaraev, K. I., and Thomas, J. M., *J. Chem. Soc. Faraday Trans.* **86,** 581 (1990).
10. Williams, C., Makarova, M. A., Malysheva, L. V., Paukshtis, E. A., Thomas, J. M., and Zamaraev, K. I., *J. Chem. Soc. Faraday Trans.* **86,** 3473 (1990).
11. Williams, C., Makarova, M. A., Malysheva, L. V., Paukshtis, E. A., Talsi, E. P., Thomas, J. M., and Zamaraev, K. I., *J. Catal.* **127,** 377 (1991).
12. Stepanov, A. G., Ramannikov, V. N., and Zamaraev, K. I., *Catal. Lett.* **13,** 395 (1992).
13. Stepanov, A. G., Zamaraev, K. I., and Thomas, J. M., *Catal. Lett.* **13,** 407 (1992).
14. Hughes, T. R., and White, H. M., *J. Phys. Chem.* **71,** 2192 (1967).
15. Paukshtis, E. A., and Yurchenko, E. N., *Uspekh. Khim.* **52,** 426 (1983).
16. (a) Pimentel, G. C., and McClellan, A. L., "The Hydrogen Bond." San Fransisco, 1960; (b) "The Hydrogen Bond" (N. D. Sokolov, Ed.). Nauka, Moscow, 1981.
17. Kustov, L. M., Kazansky, V. B., Beran, S., Kubelkova, L., and Jiru, P., *J. Phys. Chem.* **91,** 5247, 1987.
18. Knözinger, H., *in* "Acid–Base Catalysis," (K. Tanabe, H. Hattori, T. Yamaguchi, and T. Tanaka Eds.). Tokyo, 1988.
19. Paukshtis, E. A., Soltanov, R. E., and Yurchenko, E. N., *React. Kinet. Catal. Lett.* **19,** 119 (1982).
20. Cardona-Martinez, N., and Dumesic, J. A., *J. Catal.* **125,** 427 (1990).
21. (a) Szymanski, H. A., "Interpreted Infrared Spectra," Vol. 2. Plenum, New York, 1966; (b) Pouchert, C. J., "Aldrich Library of Infrared Spectra." 1981.
22. Bellamy, L. J., "The Infrared Spectra of Complex Molecules." Chapman & Hall, London, 1975.
23. Paukshtis, E. A., "Infrared Spectroscopy in Heterogeneous Catalysis," p. 256. Nauka, Novosibirsk, 1992.
24. Moravek, V., and Kraus, M., *Collect. Czech. Chem. Commun.* **51,** 763 (1986).
25. Jacobs, P. A., Tielen, M., and Uytterhoeven, J. B., *J. Catal.* **50,** 98 (1977).
26. Zhorov, Yu. M., "Isomerization of Olefins," Khimia, Moscow, 1977.
27. Koubek, J., Pasek, J., and Ruzicka, V., *in* "Catalyst Deactivation" (B. Delmon and G. F. Froment, Eds.), p. 251. Elsevier, Amsterdam, 1980.
28. Moravek, V., and Kraus, M., *J. Catal.* **87,** 452 (1984).